

Case study

Experimental and numerical study of the acoustic performance of a novel composite core thermal break

Tran-Van Han ^{a,c,1}, Gayoon Lee ^{a,2}, Yun-Seong Shin ^a, Sungwoo Woo ^b, Kihak Lee ^{a,*}

^a Deep Learning Architecture Research Center, Department of Architectural Engineering, Sejong University, 209 Neungdong-ro, Gwangjin-gu, Seoul 05006, Republic of Korea

^b Ministry of the Interior and Safety, 42 Doum 6-ro, Sejong-si 30112, Republic of Korea

^c Faculty of Civil Engineering, Mien Trung University of Civil Engineering, Tuy Hoa and Danang, Viet Nam

ARTICLE INFO

Keywords:

Thermal bridges
Thermal break
Airborne sound insulation
Vibro-acoustic analysis
Finite element method
Wall intersection

ABSTRACT

This study assesses the acoustic performance of a novel thermal break system with composite cores through both experimental testing and Finite element (FE) analysis. The research explores the effects of varying the thicknesses of key materials, including Expanded Polystyrene (EPS), Cellulose Fiber Reinforced Cement (CRC) boards, and Melamine foam, on sound insulation while maintaining a constant overall thickness of the thermal break. Results show that reducing EPS thickness and increasing CRC or Melamine foam thickness by 12 mm, along with strategic layering of Melamine with CRC boards, enhances sound insulation by 2–5 decibels (dB). The configuration with the thickest Melamine foam layer achieved the highest sound insulation improvement, ranging from 2 to 6 dB over other configurations. Additionally, FE vibro-acoustic analysis proved to be a reliable predictor of acoustic performance, closely aligning with experimental data. A parametric study further revealed a nearly linear correlation between EPS layer thickness and sound insulation efficacy. These findings underscore the crucial role of material selection and strategic layering in designing thermal breaks that effectively balance sound and thermal insulation, contributing to improved environmental quality and occupant comfort in buildings.

1. Introduction

Sustainable construction integrates innovative materials and strategies to minimize environmental impact while enhancing energy efficiency and occupant comfort. Recent advancements in sustainable construction materials, such as the use of crumb rubber and mine tailings in concrete, highlight the potential for reducing waste and improving thermal performance [1,2]. These materials, studied extensively, offer a promising pathway to lower the ecological footprint of buildings by repurposing industrial byproducts and enhancing insulation properties. On the other hand, energy consumption in the building sector poses a significant challenge, accounting for 40 % of global energy use [3]. This consumption is rising rapidly due to increasing demands for heating and cooling, which contribute substantially to carbon emissions. The issue is particularly acute in regions like Korea, where stark seasonal

* Corresponding author.

E-mail address: kihaklee@sejong.ac.kr (K. Lee).

¹ 0000-0001-7782-0785

² 0000-0001-6824-8019

temperature differences drive substantial energy needs. A major contributor to this energy inefficiency is building facades, which can account for more than half of a building's energy demand [4]. Addressing these challenges requires a dual focus: leveraging sustainable materials to improve building performance and tackling energy loss through advanced design solutions.

Thermal bridges—junctions where structural elements such as roofs, floors, and walls meet—are well-known for undermining the thermal performance of buildings [5,6]. These bridges lead to increased heat loss in winter and heat gain in summer, which exacerbates energy inefficiency and can lower interior surface temperatures, increasing the risk of condensation, mold growth, and reduced indoor air quality [7]. Addressing the thermal transmittance of these bridges is crucial for enhancing energy efficiency and maintaining a healthy indoor environment.

While the use of thermal breaks has been widely studied as a solution for mitigating thermal bridges, particularly in balcony structures, research on effective solutions for addressing thermal bridges at concrete wall connections remains limited. This study introduces a novel vertical composite core thermal break designed specifically for the junction between outer and inner concrete walls in buildings, as depicted in Fig. 1a. The innovative design minimizes direct contact between the walls by using connectors made of Ultra-High-Performance Concrete (UHPC), reinforced with stainless steel bars. The UHPC connectors, shown in Fig. 1b and c, were selected for their superior thermal insulation properties and high compressive strength compared to traditional concrete [8–10]. These connectors link the outer and inner walls, with insulating materials filling the gaps to effectively reduce heat transfer. This novel thermal break design not only stabilizes internal building temperatures and enhances energy efficiency but also ensures robust structural connections [11–13].

In addition to addressing thermal performance, environmental performance research in building design must also consider sound attenuation, which is critical for occupant comfort, especially in urban environments. In Korea, residential noise regulations are strictly enforced under Article 2 of the Environmental Policy Framework Act's Enforcement Decree and Article 9 of the Housing Construction Standards, which limit noise levels to 65 dBA [14,15]. Exceeding this limit necessitates soundproofing interventions, underscoring the importance of the acoustic properties of insulation materials.

Numerous studies have explored the acoustic properties of insulation materials. For example, Hongisto et al. [16] compared the acoustic properties of thirteen commercially available thermal insulator types. The dynamic stiffness per unit area of various insulators was studied by Urbán et al. [17], while Berardi and Iannace [18], Moretti et al. [19] examined the sound absorption coefficients of thermal insulators. The microstructure of different thermal insulation materials significantly influences their acoustic characteristics. Materials with higher airflow resistivity generally exhibit diminished sound absorption capabilities [20]. Enhanced sound absorption, which positively contributes to the sound reduction index, is particularly effective when insulation is placed between two building walls [21]. However, sandwich wall constructions and other similar configurations often suffer from poor sound insulation at resonance frequencies, typically within the 100–3150 Hz range [22]. Similar resonance issues are also observed in floating floors, where increased dynamic stiffness per unit area is associated with reduced impact sound insulation [23].

While extensive research has focused on the thermal insulation properties of thermal breaks, their sound insulation performance remains largely unexplored, despite its crucial role in indoor environmental quality and occupant comfort. Noise transmission within buildings, particularly from external and adjacent sources, predominantly occurs through walls, where thermal breaks can act as weak acoustic points, potentially reducing overall sound insulation. To address this gap, this study systematically investigates the airborne sound insulation performance of thermal breaks, specifically at wall junctions, where their acoustic impact is most significant.

The novelty of this study lies in the development and evaluation of a novel thermal break system designed for wall intersections between outer and inner concrete walls in buildings. Unlike conventional studies that primarily focus on thermal insulation, this research examines the airborne sound insulation properties of thermal breaks—an aspect often overlooked in previous works. By integrating experimental testing and numerical modeling, the study systematically evaluates the acoustic performance of different thermal insulation layer configurations. The findings establish a strategic approach for enhancing sound insulation, providing valuable insights for the design of multifunctional thermal breaks that optimize both thermal and acoustic efficiency in modern building

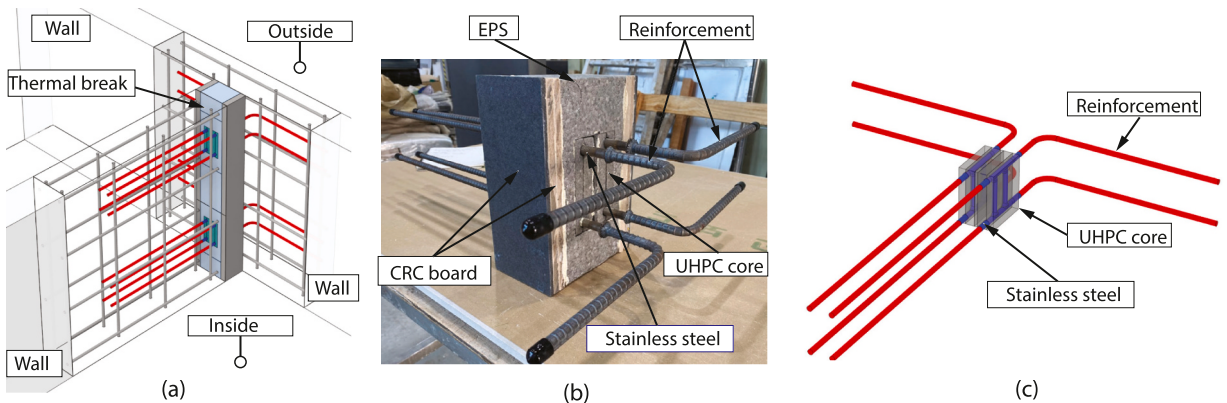


Fig. 1. The concept of the thermal break at the wall intersection: (a) Thermal break inside the building; (b) The actual image of the thermal break; and (c) the UHPC core.

applications.

The structure of the paper is organized as follows: [Section 2](#) explains the experimental programs in detail. [Section 3](#) discusses the experimental results. [Section 4](#) outlines the finite element (FE) modeling strategy, its validation with experimental data, and a parametric study based on finite element analysis (FEA) of different configurations of the novel thermal break. Finally, [Section 5](#) summarizes the key conclusions, highlighting the implications of the results and providing recommendations for future research.

2. Experimental program

The measurements were conducted at the Acoustic Testing Complex of Korea Conformity Laboratories (KCL) in South Korea.

2.1. Materials

The thermal break system consists of multiple insulating materials and includes a UHPC core. However, this study focuses solely on the insulating layers, excluding the UHPC core from the investigation. The system comprises three insulation materials: Cellulose Fiber Reinforced Cement Board (CRC board, denoted as *C*), Expanded Polystyrene (EPS, denoted as *E*), and Melamine Foam (denoted as *M*).

The densities of CRC board, EPS, and Melamine foam are 1400 kg/m^3 , 31 kg/m^3 , and 9 kg/m^3 , respectively, while their Young's moduli are 15000 MPa and 8 MPa for CRC board and EPS, respectively [24]. A summary of these material properties is provided in [Table 1](#).

The Melamine foam used in this study is an open-cell foam made of melamine resin [25]. Its sound absorption characteristics, determined according to DIN EN ISO 354 [26], are highly dependent on thickness. However, the specific values used in this study (24 mm and 36 mm) were not explicitly listed in the manufacturer's technical datasheet [25] and were instead interpolated from available data. The frequency-dependent sound absorption properties are presented in [Fig. 2](#). Additionally, the density and speed of sound in air were assumed to be 1.2 kg/m^3 and 340 m/s, respectively [27].

The selection and layering sequence of CRC board, EPS, and Melamine foam in the thermal break system were determined based on structural, thermal, and acoustic performance requirements. CRC board was chosen as the primary structural component due to its high compressive strength and rigidity, making it suitable as the outermost layer to enhance mechanical stability, protect inner insulation layers, and resist external loads. Previous studies have shown that integrating CRC significantly improves the overall load-bearing capacity of the connection [24]. EPS was selected for its low thermal conductivity and lightweight nature, providing effective thermal insulation. Its closed-cell structure minimizes heat transfer while maintaining structural efficiency, while its rigid, thermoplastic composition ensures water resistance and durability [28,29].

For acoustic performance, Melamine foam was incorporated to enhance sound insulation due to its highly porous structure, which effectively absorbs sound, particularly in the mid-to-high frequency range [30]. The placement and thickness of the Melamine layer were optimized to balance bending stiffness and sound absorption. The layering sequence was designed to maximize both stiffness and sound reduction performance, as higher bending stiffness improves low-frequency sound insulation, while strategically positioned Melamine foam enhances high-frequency absorption. Additionally, CRC board was included to provide fire resistance [31] and durability, ensuring long-term performance under real-world conditions. CRC panels further extend the fire resistance period to approximately three hours in the event of a fire [32,33]. These design considerations aim to achieve an optimal balance between mechanical strength, thermal insulation, and acoustic performance, making the thermal break system well-suited for structural applications.

2.2. Specimen description

Five types of the novel thermal break, along with a standard 404 mm-thick soundproofing wall designated as the reference (REF), were evaluated, as shown in [Table 2](#). The five types of the novel thermal break were categorized into two groups: Group 1 included specimens with an EPS core and CRC layers (C12/C12/E152 and C6/C12/C12/E140). Group 2 comprised configurations with an EPS core, external CRC layers, and Melamine foam layers (C12/M18/E140, C12/M12/C6/E140, and C12/M6/C6/E140).

The nomenclature for the thermal break samples specifies the layered composition and thickness of each insulation material, with EPS as the central layer. For instance, the specimen labeled C12/M12/C6/E140 consists of a core EPS layer, 140 mm thick, surrounded by layers of 12 mm CRC board, 12 mm Melamine foam, and 6 mm CRC board, arranged from exterior to interior, as illustrated in [Fig. 3e](#). In comparison, the REF404 sample represents to the benchmark soundproofing wall with a 404 mm thickness, as shown in [Fig. 3a](#). The composition of the thermal insulation layers for all six wall types is depicted in [Fig. 3](#).

Each thermal break specimen was constructed with a thickness of 200 mm. The specimens were evaluated with two different

Table 1
Material properties.

No.	Material	Young's modulus (MPa)	Poisson's ratio	Mass density (kg/m^3)	Speed of sound (m/s)
1	Expanded Polystyrene (CRC)	15000	0.16	1400	–
2	Expanded Polystyrene (EPS)	8	0.3	31	–
3	Melamine	0.67	0.3	9	–
4	Air	–	–	1.20	340

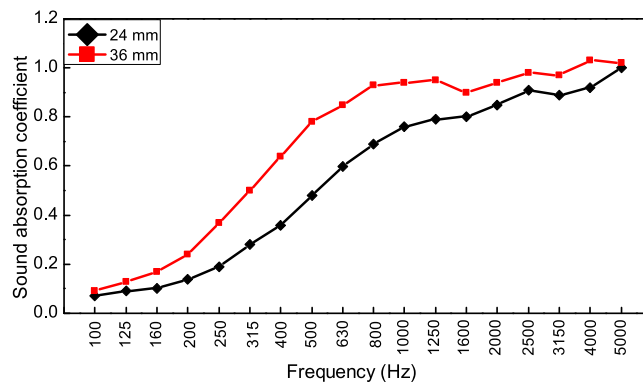


Fig. 2. Dependence of sound absorption coefficient on thickness for melamine.

Table 2

Detailed composition of the test specimens.

Wall type	Nomenclature	Thickness (mm)	Composition
Reference wall	REF 404	404	—
Thermal break Group 1	C12/C12/E152	200	C12mm+C12mm+E152mm+C12mm+C12mm
	C6/C12/C12/E140	200	C6mm+C12mm+C12mm+E140mm+C12mm+C12mm+C6mm
Thermal break Group 2	C12/M18/E140	200	C12mm+M18mm+E140mm+M18mm+C12mm
	C12/M12/C6/E140	200	C12mm+M12mm+C6mm+E140mm+C6mm+M12mm+C12mm
	C12/M6/C6/M6/E140	200	C12mm+M6mm+C6mm+M6mm+E140mm+M6mm+C6mm+M6mm+C12mm

Note: Each composition was tested with two specimens having areas of 1.82 m² and 10.06 m².

surface area dimensions (height × width): 2780×3620 mm (10.06 m²) for Test 1 and 1480×1230 mm (1.82 m²) for Test 2. The surface density and bending stiffness values [34] for these specimens are provided in Table 3.

The fabrication process of the test specimen, as depicted in Fig. 4, follows a series of key steps. First, the specimen is assembled by bonding the layers of CRC, EPS, and Melamine using adhesive. Once the layers are securely attached, the specimen is placed into the filler wall structure. Steel angles and screws are used to firmly connect the specimen to the filler wall.

To minimize flanking transmission and ensure that sound insulation measurements accurately reflect the specimen's performance, all gaps between the specimen and the filler wall were sealed with acoustic sealing strips made of polyurethane foam. After the assembly was completed, the unit was transported to the testing room using a rail system.

Interface bonding was ensured using construction adhesives; however, variations in adhesion thickness, minor voids, and pressure distribution during fabrication may have introduced local inconsistencies in acoustic impedance. At low frequencies, wave propagation is primarily governed by bulk material properties, whereas at mid and high frequencies, interface stiffness and bonding conditions strongly influence transmission loss [35]. These factors were considered when interpreting the experimental results and comparing them with numerical predictions.

2.3. Testing method

Specimens of the novel thermal breaks and reference walls were tested in a facility with two reverberation rooms, measuring 53.0 m³ and 58.4 m³ for the source and receiving rooms, respectively. To prevent flanking transmission, the rooms were acoustically isolated, with additional sound-insulating lining applied to the walls and ceiling of the receiving room. Diffusers were placed on the walls of both chambers to create a diffuse sound field, simulating actual conditions where sound approaches the sample from multiple directions. The entire setup, including measurement procedures and equipment, conformed to EN ISO 10140–4:2021 standards [36].

In this test, for sound insulation testing, directional speakers (JBL, SRX-835P) served as the sound source, while ten non-directional microphones (GRAS Type 146AE) were placed in both the source and receiving rooms. Data was analyzed using a multi-channel measuring device (Rion, SA-02M12). Fig. 5 illustrates the experimental setup in the reverberation rooms, and Fig. 6 shows an actual image of the acoustic insulation tests.

Sound pressure levels in the source and receiving rooms were measured simultaneously after white noise was generated. Based on these measurements, airborne sound insulation values were calculated and evaluated.

2.4. Evaluation of airborne sound insulation

The sound insulation performance of the specimens was evaluated in accordance with ISO 10140–2:2021 standards [37] in a controlled laboratory environment. Sound pressure levels (SPL) were measured simultaneously in both the source and receiving rooms following the introduction of white noise through laboratory-installed speakers. These measurements were taken in one-third octave

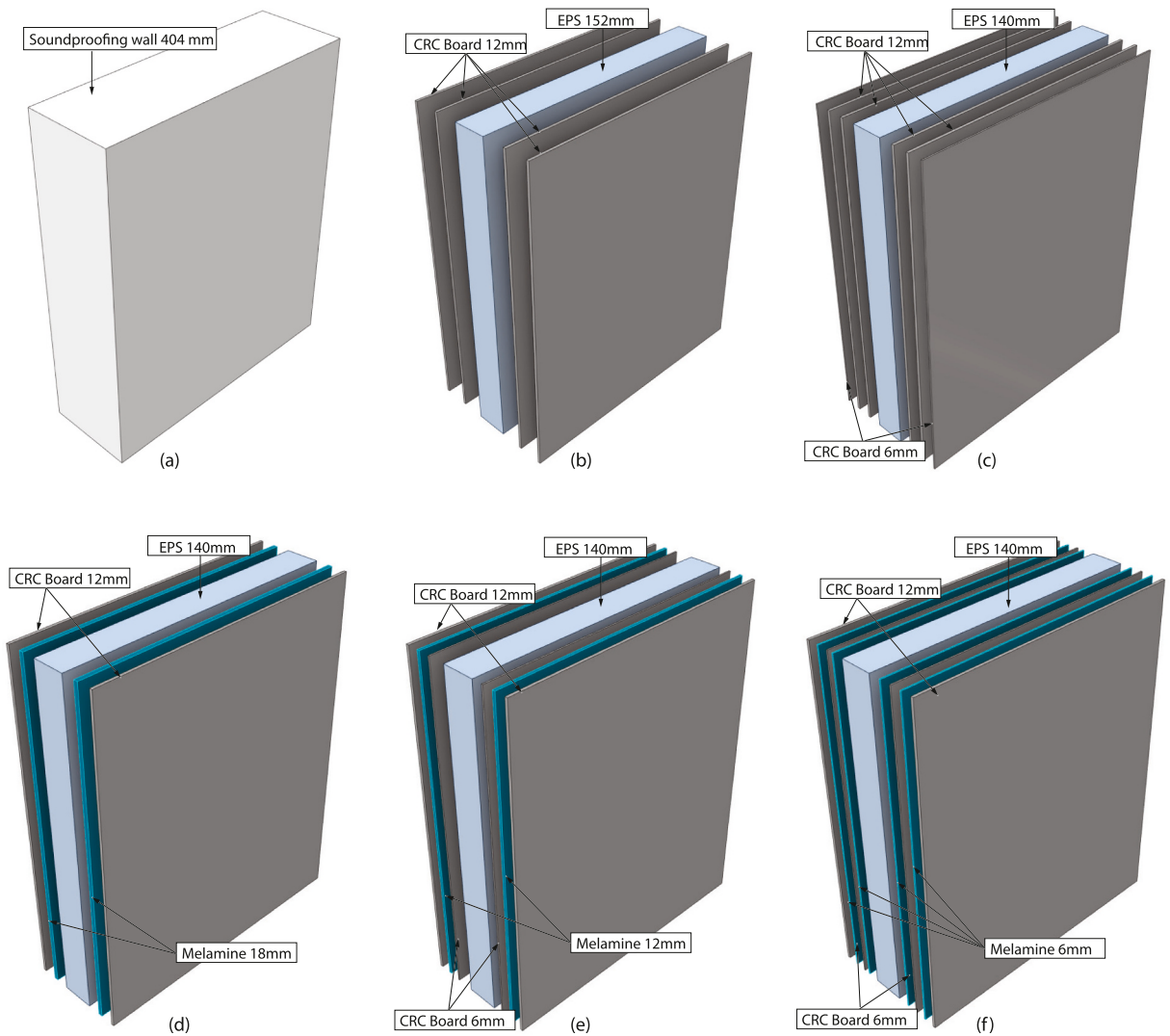


Fig. 3. Composition of the specimens: (a) the reference (REF) wall; (b) C12/C12/E152; (c) C6/C12/C12/E140; (d) C12/M18/E140; (e) C12/M12/C6/E140; and (f) C12/M6/C6/M6/E140.

Table 3
Surface density and bending stiffness values of the specimens.

No.	Wall type	Thickness (mm)	Surface density (kg/m^2)	Bending stiffness (MN.m)
1	REF404	404	–	–
2	C12/C12/E152	200	71.91	5.61
3	C6/C12/C12/E140	200	88.34	4.80
4	C12/M18/E140	200	38.26	3.19
5	C12/M12/C6/E140	200	54.96	4.15
6	C12/M6/C6/M6/E140	200	54.96	4.31

bands and averaged for both rooms [38].

The difference in SPLs between the two rooms was used to derive the sound reduction index (R), which is a frequency-dependent metric. This index was then converted into the weighted sound insulation index (R_w) following the guidelines of ISO 717-1 [39]. ISO 717-1 also provides methods for applying correction factors: the C_{tr} adjustment for traffic noise, which emphasizes lower frequencies and is suitable for urban noise, low-speed rail, and specific industrial sounds ($R_w + C_{tr}$), and the C correction, which applies to high-speed traffic, residential noise, and internal building sounds ($R_w + C$).

The R_w values were calculated after calibrating the reverberation time in the receiving room [15]. The sound reduction index R [dB] was calculated across one-third octave band frequencies within the range specified by ISO 717-1 [39], as outlined in Eq. (1).

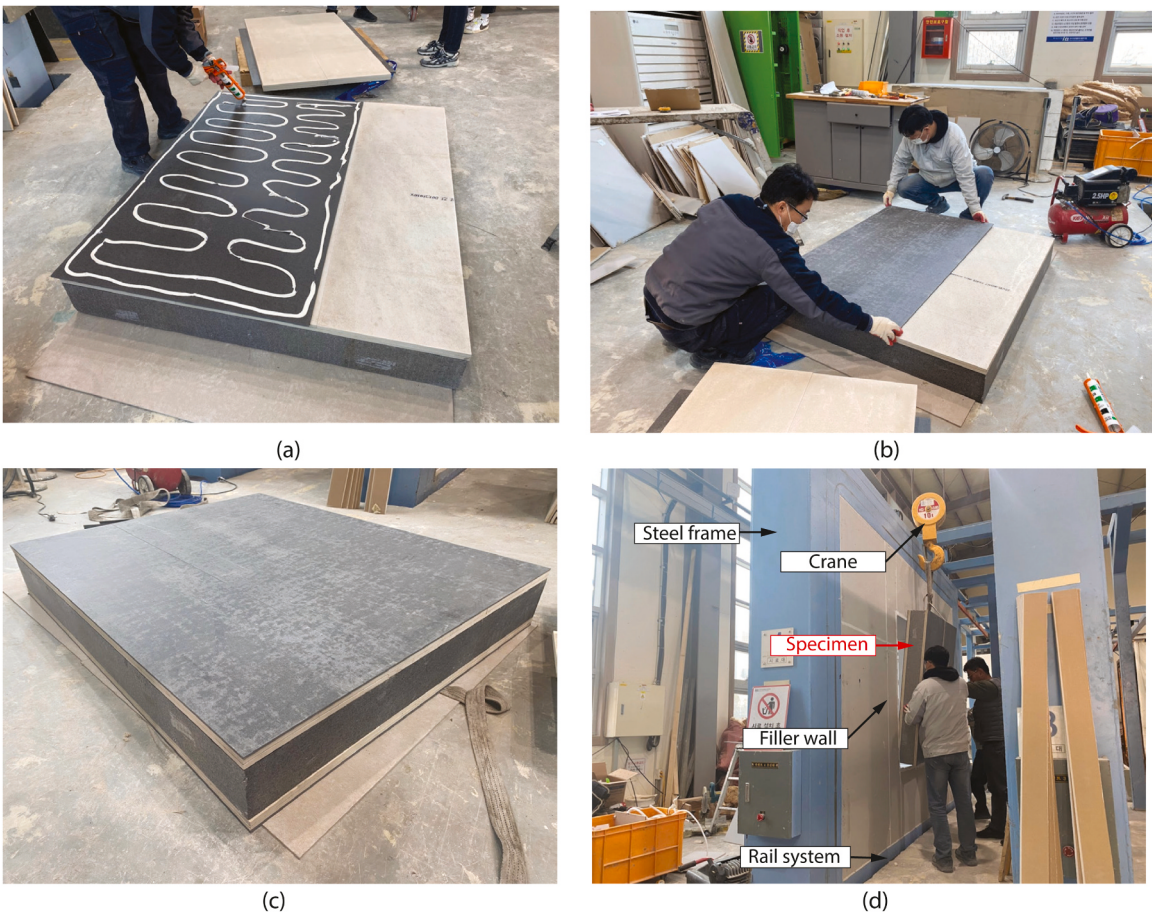


Fig. 4. Composition of the specimens: The layers of insulation are bonded with glue (a,b); Completed specimens (c); Install the specimen on the steel frame (d).

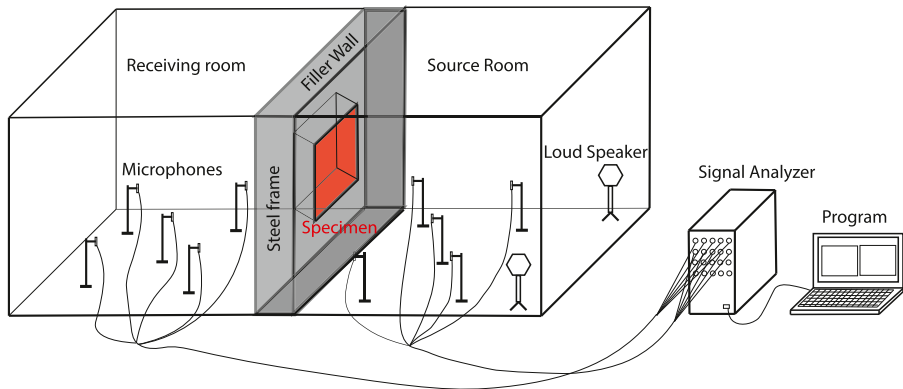


Fig. 5. Experimental instrument setup.

$$R = L_1 - L_2 + 10 \log \frac{S}{A} \quad (1)$$

Where: L_1 is the average sound pressure level in the source room in dB, L_2 is the average level in the receiving room in dB, S is the tested module's surface area in m^2 , and A is the equivalent sound absorption area in the receiving room, determined by Eq. (2). The measurements for L_1 and L_2 span frequencies from 100 Hz to 5000 Hz within one-third octave bands.

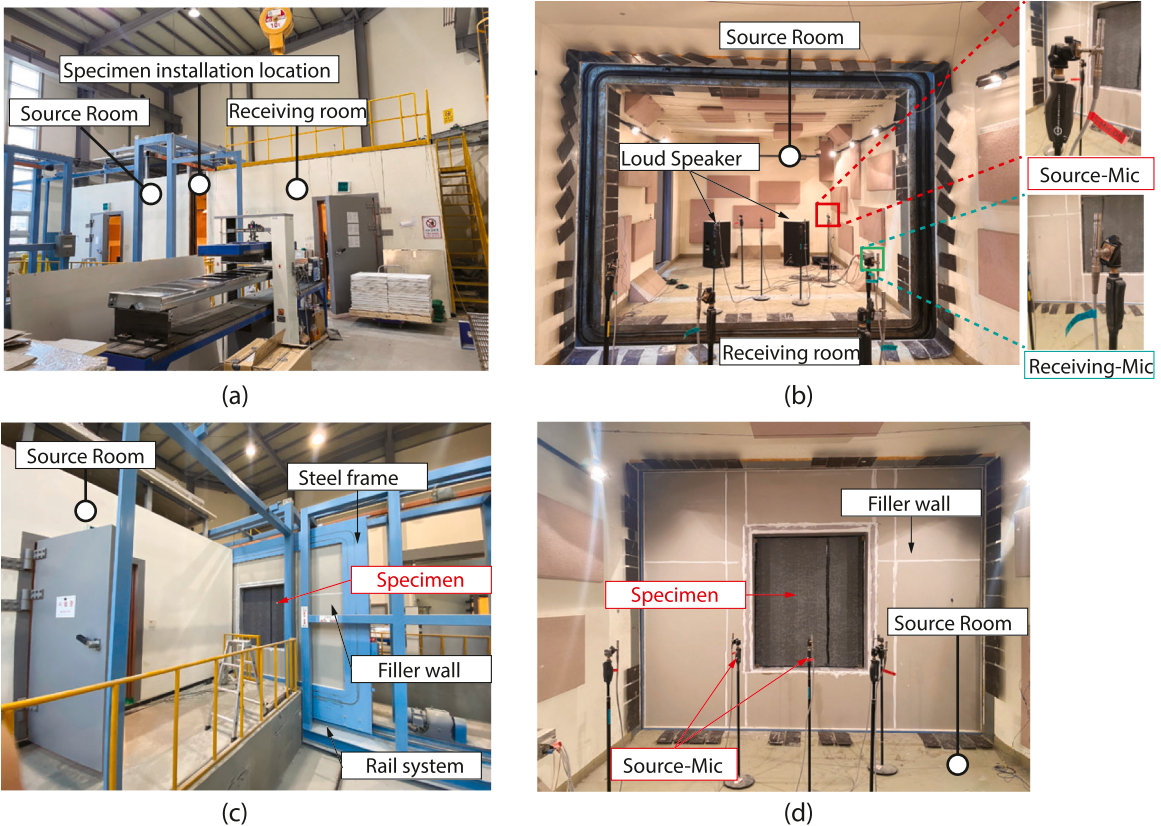


Fig. 6. Actual image of the reverberation rooms for acoustic insulation tests: (a) overall external view of the source and receiving rooms without the specimens; and (b) Inner view of the source and receiving rooms without the specimens; (c) Install the specimens between the two rooms using a rail system; and (d) Complete specimen installation.

$$A = \frac{0.163V}{T} \quad (2)$$

where: V: the volume of the receiving room in m^3 ; T: the reverberation time of the receiving room in s. Reverberation time was determined using two averaged decay signals from the decay range of -5 to -25 dB in each measurement [16].

3. Experimental results and discussion

All tests assessing the acoustic performance of thermal insulation solutions for thermal bridges complied with the ISO 10140-2 international standard [37]. The evaluations included a standard soundproofing wall of 404 mm thickness and ten specimens of the new thermal break, each 200 mm thick. The sound reduction index, standardized across the industry, was determined in third-octave bands from 100 Hz to 5000 Hz.

Comments on the results consider the behavior of theoretical sound insulation. Idealized curves represent the general behavior of the sound reduction index for a single uniform partition. The transmission loss curves can be divided into three regions: stiffness-controlled, mass-controlled, and damping-controlled [34]. In these curves, specific frequencies and regions are defined to characterize the behavior of sound insulation [40]. The critical frequency f_c typically corresponds to a dip or minimum in the sound reduction index within the coincidence region, and its value is given by Eq. (3) [41,42].

$$f_c = \frac{c^2}{1.8h\sqrt{\frac{E}{\rho_m(1-\nu^2)}}} \quad (3)$$

Where: c is the sound velocity in the air (343 m/s); E is the Young's modulus; ν is the Poisson's coefficient; ρ_m is the medium density of the wall; h is the thickness of the wall.

The measured critical frequencies were taken to be the frequencies in the coincidence region where the sound reduction index was minimum. The results are measured at frequencies of one-third of the octave band [40].

3.1. Sound insulation performance of thermal insulation solutions

The experimental investigation into different thermal insulation solutions, as well as the standard soundproofing wall, revealed significant trends in sound insulation performance. The results, summarized in Table 3 and Fig. 7, show that the REF specimen consistently achieved a higher sound reduction index across the 100–5000 Hz range in both Test 1 (Fig. 7a) and Test 2 (Fig. 7b). The findings indicate that sound insulation capabilities are generally enhanced in specimens with larger surface areas.

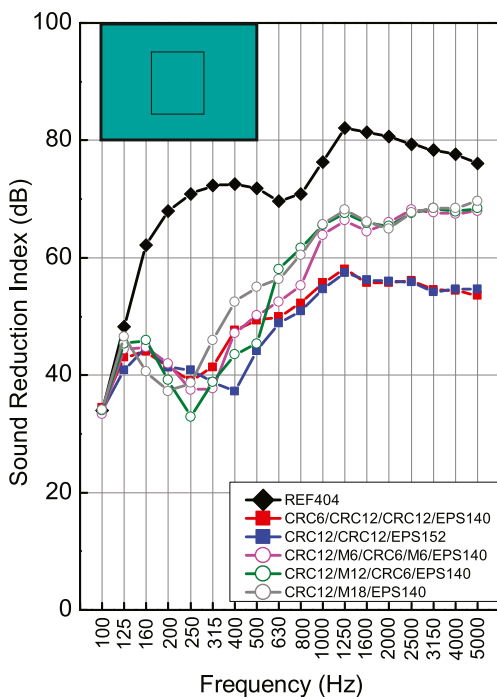
The sound insulation performance of the thermal break specimens exhibited consistent behavior across different frequency regions. The combination of EPS cores, CRC layers, and Melamine foam played a key role in determining stiffness, mass, and damping effects, with each material contributing differently across specific frequency ranges. Based on Fig. 7b, the general observations across the thermal break specimens are as follows:

1. Stiffness-controlled region (low frequencies: below 250 Hz)

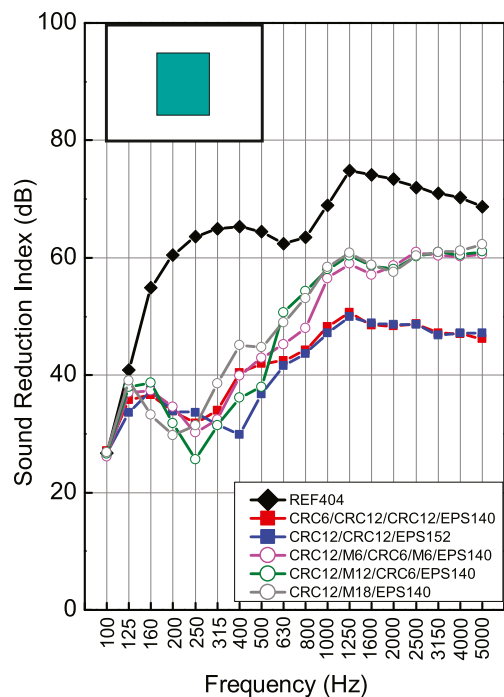
- In the low-frequency range (100–250 Hz), sound insulation is primarily influenced by the bending stiffness of all layers and the sound absorption properties of the Melamine foam layer. Specimens composed solely of CRC and EPS layers, such as C6/C12/C12/E140 (bending stiffness = 4.8 MN.m) and C12/C12/E152 (5.61 MN.m), exhibited comparable acoustic performance, indicating that bending stiffness plays a dominant role in this frequency range.
- Specimens incorporating the thickest Melamine foam (36 mm), such as C12/M18/E140, exhibited the lowest sound insulation in the stiffness-controlled frequency range. This reduction in performance was attributed to the lower stiffness of Melamine foam compared to CRC and EPS. Notably, C12/M18/E140, which had the lowest bending stiffness (3.19 MN.m), recorded the weakest acoustic performance, with sound reduction indices of 25.8 dB at 160 Hz and 22.4 dB at 200 Hz.
- In contrast, specimens with a total Melamine foam thickness of 24 mm, such as C12/M6/C6/M6/E140 (bending stiffness = 4.31 MN.m) and C12/M12/C6/E140 (4.15 MN.m), achieved the highest sound reduction indices. Despite having slightly lower bending stiffness than CRC-EPS-based specimens like C6/C12/C12/E140 (4.8 MN.m) and C12/C12/E152 (5.61 MN.m), these configurations outperformed them in terms of sound insulation. These findings highlight the necessity of balancing bending stiffness and Melamine foam thickness to optimize low-frequency sound insulation.

2. Mass-controlled region (mid frequencies: 250 Hz–1250 Hz)

- In the mid-frequency range, where mass plays a critical role, C6/C12/C12/E140, with a mass per unit area of 88.34 kg/m², outperformed lighter specimens like C12/C12/E152 (71.91 kg/m²). This was reflected in the 10.5 dB improvement at 400 Hz for C6/C12/C12/E140 compared to C12/C12/E152, highlighting the impact of surface mass on mid-frequency sound insulation.



(a) Test 1 ($S=10.06\text{ m}^2$).



(b) Test 2 ($S=1.82\text{ m}^2$).

Fig. 7. Sound insulation performance of specimens with different surface areas.

- Similarly, thicker Melamine foam layers contributed positively in this region. For example, C12/M18/E140 exhibited sound insulation improvements ranging from 8.9 to 9.7 dB between 250 Hz and 500 Hz compared to C12/M12/C6/E140. This demonstrates the effectiveness of Melamine foam in enhancing sound insulation in the mid-frequency range, owing to its acoustic absorption properties.
3. Damping-controlled region (high frequencies: 1250 Hz–5000 Hz)
- In the high-frequency range, where damping effects dominate, specimens incorporating Melamine foam performed better than those relying solely on CRC and EPS layers. C12/M12/C6/E140 exhibited up to a 14.9 dB higher sound insulation at 5000 Hz compared to C6/C12/C12/E140, showcasing the superior sound-absorbing properties of Melamine foam.
 - Interestingly, variations in Melamine foam thickness had minimal impact on high-frequency performance. For instance, the difference in sound insulation between C12/M18/E140 and C12/M12/C6/E140 was only 1.2 dB at 5000 Hz, suggesting that the sound-absorbing properties of Melamine foam remain effective regardless of minor changes in thickness.

Comparative analysis of group 1 (EPS core with external CRC layers) and Group 2 (EPS core with CRC and Melamine foam layers) specimens:

- Group 1 (EPS core with external CRC layers) demonstrated superior sound insulation in the stiffness-controlled and mass-controlled regions. For example, C6/C12/C12/E140 outperformed C12/M12/C6/E140 by 6.2 dB at 250 Hz due to its higher stiffness, and it also showed better performance in the mid-frequency range, where its greater surface mass resulted in up to a 4.0 dB improvement. However, Group 1 specimens underperformed in the high-frequency range, indicating the limited damping properties of CRC.
- Group 2 (EPS core with CRC and Melamine foam layers) exhibited superior sound insulation in the high-frequency range, where Melamine foam's sound-absorbing properties were most effective. For example, C12/M18/E140 showed a 4–5 dB improvement in the high-frequency region compared to CRC-based specimens. While Group 2 specimens performed well in the mass-controlled region, they generally underperformed at lower frequencies, emphasizing the trade-off between stiffness and damping.

Overall, the experimental results highlight the complementary roles of CRC and Melamine foam in enhancing sound insulation across different frequency ranges. CRC-based specimens (Group 1) performed best at lower frequencies due to their stiffness and mass, while Melamine foam-based specimens (Group 2) excelled at higher frequencies due to their superior damping properties. The most balanced performance was observed in specimens like C12/M18/E140, which effectively combined both CRC and Melamine foam to optimize sound insulation across a wide frequency spectrum.

3.2. Comparison of sound insulation performance using single rating method

To further evaluate the acoustic performance of the ten thermal break specimens, the single rating method, focusing on R_w and $R_w + C$, was applied as specified in ISO 717-1 [39] and KS F 2862 [43]. The methodology for calculating R_w values is detailed in the Appendix A, and Table 4 and Fig. 8 provide a comparative analysis of the sound insulation performance of the thermal insulation specimens versus the conventional soundproofing wall.

Overall, the R_w and $R_w + C$ values of the REF specimen significantly exceeded those of all the thermal break specimens in both Test 1 and Test 2, with a difference ranging from 16 to 23 dB. According to the acoustic performance classification, the REF specimen is categorized as level 2, while the thermal break specimens fall between levels 3 and 4, showing an overall lower performance.

Also, the results indicate that specimens with larger surface areas exhibit superior sound insulation performance. Specifically, the 10.06 m² specimens in Test 1 demonstrated enhanced sound insulation compared to the 1.82 m² specimens in Test 2, primarily due to three key factors.

First, larger specimens have a lower perimeter-to-area ratio, which mitigates edge effects [44] by reducing sound leakage and diffraction at the boundaries. This results in an increased sound reduction index (R) and higher single-number quantities (R_w , $R_w + C$), with an observed improvement of 7–8 dB in Test 1 specimens relative to those in Test 2 (see Table 4).

Table 4

The overall acoustic performance of the specimens.

Test	Area(m ²)	Wall type	Thickness (mm)	R_w (dB)	C (dB)	C_{tr} (dB)	$R_w + C$ (dB)	Level
1	10.06	REF404	404	71	-9	-17	62	2
		C12/C12/E152	200	50	-2	-5	48	4
		C6/C12/C12/E140	200	52	-1	-5	51	4
		C12/M18/E140	200	55	-2	-7	53	3
		C12/M12/C6/E140	200	50	-1	-5	49	4
		C12/M6/C6/M6/E140	200	53	-2	-6	51	4
2	1.82	REF404	404	64	-9	-18	55	3
		C12/C12/E152	200	42	-1	-4	41	N.G
		C6/C12/C12/E140	200	45	-2	-5	43	N.G
		C12/M18/E140	200	48	-3	-8	45	N.G
		C12/M12/C6/E140	200	43	-2	-6	41	N.G
		C12/M6/C6/M6/E140	200	46	-2	-6	44	N.G

Note: N.G: Not given

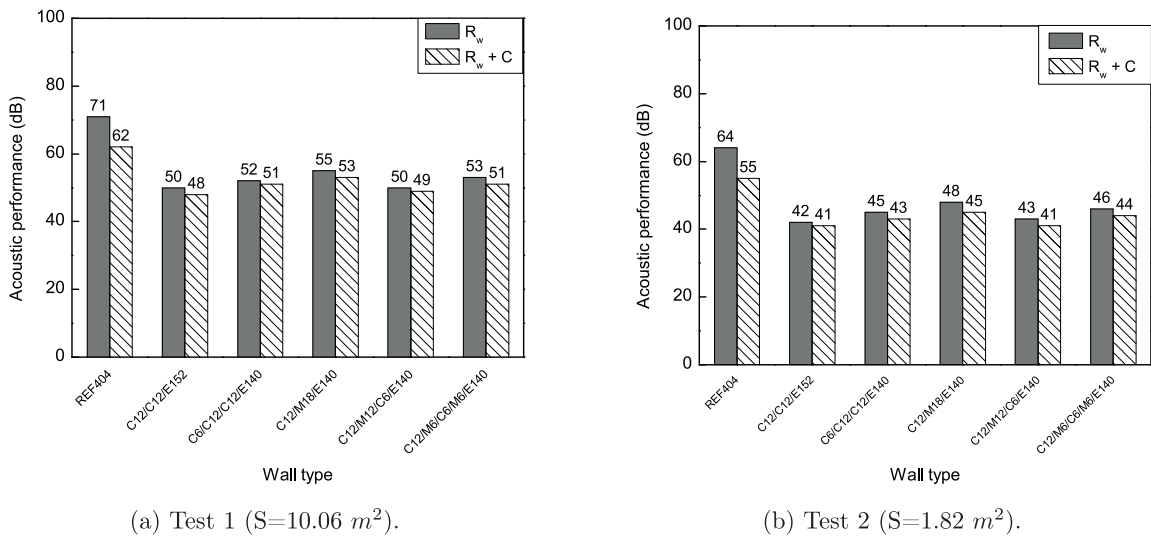


Fig. 8. The overall acoustic performance of the specimens with different surface areas.

Second, flanking transmission [34], where sound propagates through structural paths or gaps at the edges, is more pronounced in smaller specimens. In contrast, larger specimens distribute these transmission paths over a broader area, thereby minimizing localized weaknesses.

Third, the reverberation room setup, designed to generate a diffuse sound field using diffusers, more effectively approximates uniform sound incidence for larger specimens. This facilitates more uniform sound reflection and absorption, further enhancing their sound insulation capabilities.

The evaluation of sound insulation performance using the single rating method, particularly R_w and $R_w + C$, highlighted several key trends across the tested specimens.

1. In Group 1, which included specimens with EPS cores and external CRC layers, the specimen C6/C12/C12/E140 consistently outperformed C12/C12/E152 in terms of both R_w and $R_w + C$. Across both Test 1 and Test 2, C6/C12/C12/E140 exhibited an improvement of 2–3 dB in these metrics. This performance increase is attributed to the combination of reducing EPS thickness and adding an extra 12 mm CRC layer, which increased the overall stiffness and mass of the wall. The additional mass provided by the CRC layers is a crucial factor in enhancing sound insulation, especially at lower frequencies, as reflected by the improved single rating values.
2. In Group 2, where Melamine foam was integrated with EPS cores and CRC layers, the results showed a clear advantage in the mid-to-high frequency range. The specimen C12/M18/E140, which featured a thicker 18 mm Melamine foam layer, achieved a 4–5 dB improvement in both R_w and $R_w + C$ values compared to C12/M12/C6/E140. This increase can be attributed to the enhanced sound-absorbing properties of Melamine foam, which is particularly effective at higher frequencies. The foam's ability to absorb sound led to a significant increase in overall sound insulation performance across a broader frequency spectrum.
3. A significant improvement in sound insulation was observed in the configuration C12/M6/C6/M6/E140, which incorporates four layers of Melamine foam, compared to C12/M12/C6/E140, which contains only two Melamine layers. Despite both configurations having the same total Melamine foam thickness, C12/M6/C6/M6/E140 exhibited a 2–3 dB increase in both R_w and $R_w + C$ values. This improvement is attributed to the increased number of interfaces between Melamine foam and CRC boards, which create multiple impedance mismatches, enhancing wave reflection and reducing direct sound transmission [35]. The additional layer transitions facilitate greater energy dissipation by promoting wave scattering and absorption. These findings suggest that distributing Melamine foam into multiple thinner layers, rather than a single thicker layer, optimizes broadband sound insulation by disrupting sound propagation paths and improving acoustic attenuation. This result underscores the importance of optimizing layer distribution in multi-material configurations to maximize sound insulation performance.

In summary, the comparison of Group 1 and Group 2 specimens based on R_w and $R_w + C$ values shows that Group 1 specimens, such as C6/C12/C12/E140, performed better in low-frequency sound insulation due to their higher stiffness and mass. However, Group 2 specimens, particularly C12/M18/E140, excelled in mid-to-high frequency ranges, benefiting from the superior sound-absorbing properties of Melamine foam. Overall, while both groups showed improvements in sound insulation, Group 2's use of Melamine foam was more effective in achieving higher R_w and $R_w + C$ values, especially in applications requiring broader frequency sound insulation.

3.3. Strategies for improving thermal break design

The findings of this study provide valuable insights into optimizing the design of thermal breaks to enhance both sound and thermal insulation performance. The results highlight that material selection and layering sequence play a crucial role in achieving a balance between stiffness, mass, and sound absorption. To improve thermal break designs, a strategic combination of rigid and porous materials should be employed. CRC board, with its high stiffness and mass, is effective in improving low-frequency sound insulation, while Melamine foam enhances mid-to-high frequency absorption. The optimal layering sequence involves alternating stiff and porous materials, as demonstrated by the superior performance of multi-layered configurations such as C12/M6/C6/M6/E140.

One effective strategy for improving sound insulation while maintaining thermal performance is increasing the mass of the system without significantly affecting its thermal resistance. Since higher mass improves low-frequency sound insulation, integrating high-density yet thermally efficient composites or introducing air cavities within the structure can help disrupt sound transmission while preserving insulation properties. Additionally, the results indicate that optimizing the thickness of Melamine foam is critical, as excessive thickness reduces structural stiffness, leading to diminished low-frequency insulation. The study suggests that a total Melamine foam thickness of 24 mm provides an effective balance between absorption and stiffness.

Reducing flanking transmission is essential to ensure the effectiveness of thermal breaks in practical applications. Implementing additional acoustic sealing strips or resilient connections at the interface between the thermal break and adjacent structures can minimize sound leakage and improve overall acoustic performance.

While this study primarily focuses on sound insulation, future research should consider the thermal implications of different material combinations. The findings indicate that achieving an optimal balance between bending stiffness and damping properties is crucial for thermal break designs. Future improvements should focus on refining material layering, optimizing mass-stiffness relationships, and integrating novel materials to enhance both acoustic and thermal insulation performance in building applications.

Temperature fluctuations can significantly influence the material properties of EPS, CRC boards, and Melamine foam, including elastic modulus, density, and damping characteristics, as well as impact the structural integrity of UHPC connectors [45]. Additionally, the different materials in each layer may undergo varying degrees of thermal expansion or contraction, potentially altering their stiffness and mass—both critical factors in sound insulation. These differential thermal responses between layers could lead to internal stresses and structural integrity concerns, further affecting acoustic performance. Such variations in bending stiffness, surface mass, and sound absorption can ultimately modify the system's acoustic behavior across different frequency ranges. To enhance the robustness of thermal break designs for real-world applications, future research should evaluate the effects of temperature fluctuations on acoustic performance. Investigating materials with stable mechanical and acoustic properties over a broad temperature range or developing adaptive layering strategies to compensate for thermal expansion could help mitigate performance degradation and ensure long-term reliability.

4. Finite element modeling

4.1. Material properties

The acoustic fluid elements necessitate the specification of density and speed of sound as material properties. Air was modeled with a density of 1.20 kg/m^3 and a speed of sound of 340 m/s . The sound absorption of Melamine is depicted in Fig. 2. For structural elements, Young's modulus, density, and Poisson's ratio are presented in Table 1.

4.2. Finite element modelling

To assess the acoustic performance of the innovative UHPC core thermal break, a numerical model was constructed using Siemens

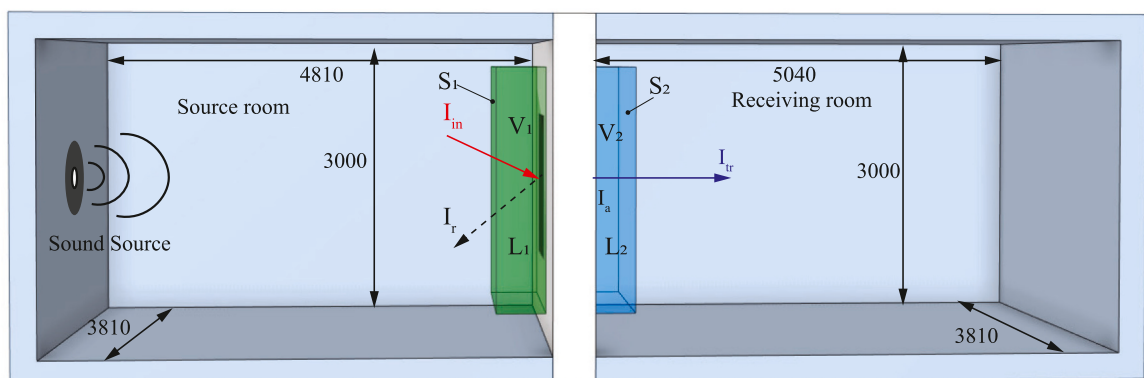


Fig. 9. Schematic of two reverberant rooms and sound transmission through their separating wall.

Simcenter 3D, version 2021.2 [46]. The challenge of predicting the sound reduction index for the wall was addressed through a vibro-acoustic FEA.

4.2.1. Model simplification

In finite element analysis, model simplification is essential to reduce computational cost, especially when simulating vibro-acoustic phenomena in large air volumes. The schematic of the 3D finite element geometric configuration for acoustic analysis is shown in Fig. 9, where I_{in} , I_r , I_a , and I_{tr} represent the incident, reflected, absorbed, and transmitted sound waves through the specimens, respectively [47]. The sound emanates from a source sound in source room, where reflections from the walls and diffuser create a diffuse sound field that randomly impacts the sample.

To optimize computational efficiency, the simulation focused on modeling the air volumes V_1 and V_2 (see Fig. 9), located near the specimens in the source and receiving rooms, respectively. A diffuse sound field was artificially generated, eliminating the need to simulate the entire air volume. Non-reflective boundary conditions were applied to surfaces S_1 and S_2 (the outer surfaces of V_1 and V_2 , except those in direct contact with the specimens) to simulate continuous sound transmission from the remaining air volume in the source room to V_1 , and from V_2 to the remaining air volume in the receiving room. The sound transmission loss R of the specimens was calculated by evaluating the difference in sound pressure levels transmitted through the specimen, with the average sound pressure levels L_1 and L_2 measured at surfaces S_1 and S_2 .

4.2.2. Finite element model

The finite element model, depicted in Fig. 10(a,b), includes air volumes V_1 and V_2 representing the source and receiving rooms, separated by a wall with varying composition and dimensions. The dimensions of V_1 and V_2 were determined by positioning the outer surfaces S_1 and S_2 500 mm away from the specimen. A diffuse sound field was generated in the model using an acoustic load consisting of distributed plane waves with a half-sphere distribution, as shown in Fig. 10(c). To accurately simulate non-reflective boundary conditions, perfectly matched layers (PML) [48], referred to as automatically matched layers (AML) in Simcenter 3D, were applied to the air surfaces S_1 and S_2 . The edges of the wall were fully constrained to keep the structure fixed during the simulation.

The vibro-acoustic analysis employed CTETRA four-node acoustic tetrahedral elements to simulate the air volumes V_1 and V_2 in the source and receiving rooms, respectively. The structural laminate of the wall was modeled using CQUAD linear four-node quadrilateral elements. To simulate the sound absorption characteristics of the Melamine insulation, an impedance coefficient was calculated based on its sound absorption coefficients, as outlined in Eq. (4) [49] and illustrated in Fig. 2.

$$\alpha = \frac{4Z_R}{\rho c} \left[\left(1 + \frac{Z_R}{\rho c} \right)^2 + \left(\frac{Z_I}{\rho c} \right)^2 \right]^{-1} \quad (4)$$

Where $Z = Z_R + j \cdot Z_I$ represents the impedance coefficient, with Z_R being the real part (resistance) and Z_I being the imaginary part (reactance). The term α denotes the acoustic absorption coefficient, while ρ refers to the density of air, and c is the speed of sound in air. According to the Simcenter 3D User Guide, for simplicity in this context, Z_I is assumed to be zero, implying that only the resistive component (Z_R) is considered for calculating acoustic impedance [49].

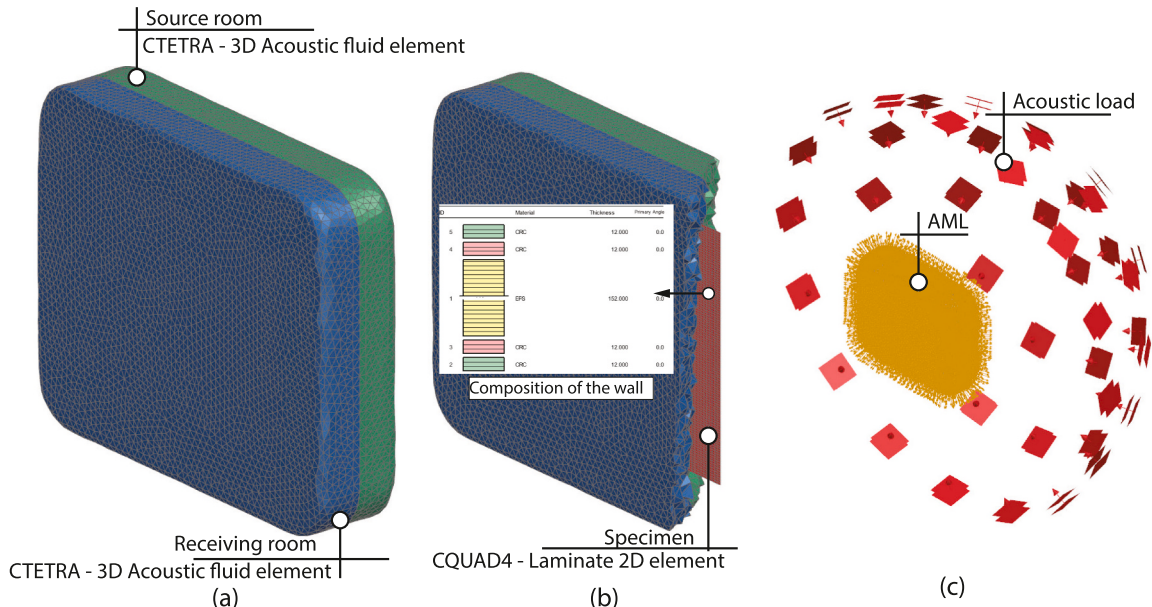


Fig. 10. Details of FE models used for numerical investigation: (a,b) FE model; (c) Boundary conditions with Automatically Matched Layers (AML) and acoustic load.

4.3. Sensitivity analysis

To optimize the mesh sizes for walls and air within the test chambers, a sensitivity analysis was conducted on the C12/C12/E152 specimen during Test 2. The simulations were performed using an AMD Ryzen 7 2700X Eight-Core Processor (3.70 GHz) with 32 GB of RAM. Two key parameters were examined: (1) varying the wall mesh size from 10 mm to 50 mm while maintaining a constant air mesh size of 100 mm, and (2) adjusting the air mesh size from 100 mm to 200 mm while keeping the wall mesh size fixed at 10 mm. The computed sound reduction index (R) values from FEA are presented in Fig. 11, demonstrating that mesh resolution significantly influences prediction accuracy, particularly at high frequencies (> 2000 Hz), emphasizing the importance of mesh refinement in acoustic simulations.

As illustrated in Figs. 11a and 12a, decreasing the wall mesh size from 50 mm to 10 mm significantly increased the number of structural elements, resulting in approximately a fourfold increase in computation time. However, this refinement substantially improved prediction accuracy. A coarse wall mesh of 50 mm exhibited poor agreement with experimental data across all frequency ranges, while a 20 mm mesh provided reasonable accuracy at low frequencies (100–250 Hz) but showed deviations at mid and high frequencies (> 250 Hz). The 10 mm mesh yielded the best performance, closely aligning with experimental results across all frequency bands. These findings highlight the necessity of wall mesh refinement for accurate numerical modeling.

Conversely, the influence of air mesh size is shown in Figs. 11b and 12b. While air mesh size variations had minimal impact on prediction accuracy at low and mid frequencies (100–2000 Hz), they significantly affected high-frequency predictions (> 2000 Hz). A coarse air mesh of 200 mm resulted in substantial discrepancies, whereas progressive refinement to 150 mm, 120 mm, and 100 mm improved agreement with experimental results. Despite this refinement, reducing the air mesh size had a negligible effect on computational time, indicating that finer air meshes are computationally efficient yet essential for maintaining accuracy in high-frequency regions.

It is noted that for high-frequency solutions in Simcenter 3D, at least six elements per wavelength are recommended for the acoustic mesh to minimize numerical dispersion errors [49]. The required air mesh size h_{air} can be estimated as:

$$h_{\text{air}} \leq \frac{\lambda}{N}, \quad \text{where } \lambda = \frac{c}{f} \quad (5)$$

where λ is the acoustic wavelength, $N = 6$, c is the speed of sound in air (340 m/s), and f is the frequency of interest.

Given that the air mesh size used in this study exceeds this threshold, numerical dispersion errors are expected in the high-frequency range. To enhance the accuracy of FE models, the *adaptive order* function [49] may be employed with coarser meshes. However, this approach should be used judiciously to ensure accuracy is maintained. Based on these findings, a wall mesh size of 10 mm and an air mesh size of 100 mm were identified as optimal, providing a balance between computational efficiency and accuracy. This configuration was adopted for all subsequent analyses to ensure reliable numerical predictions.

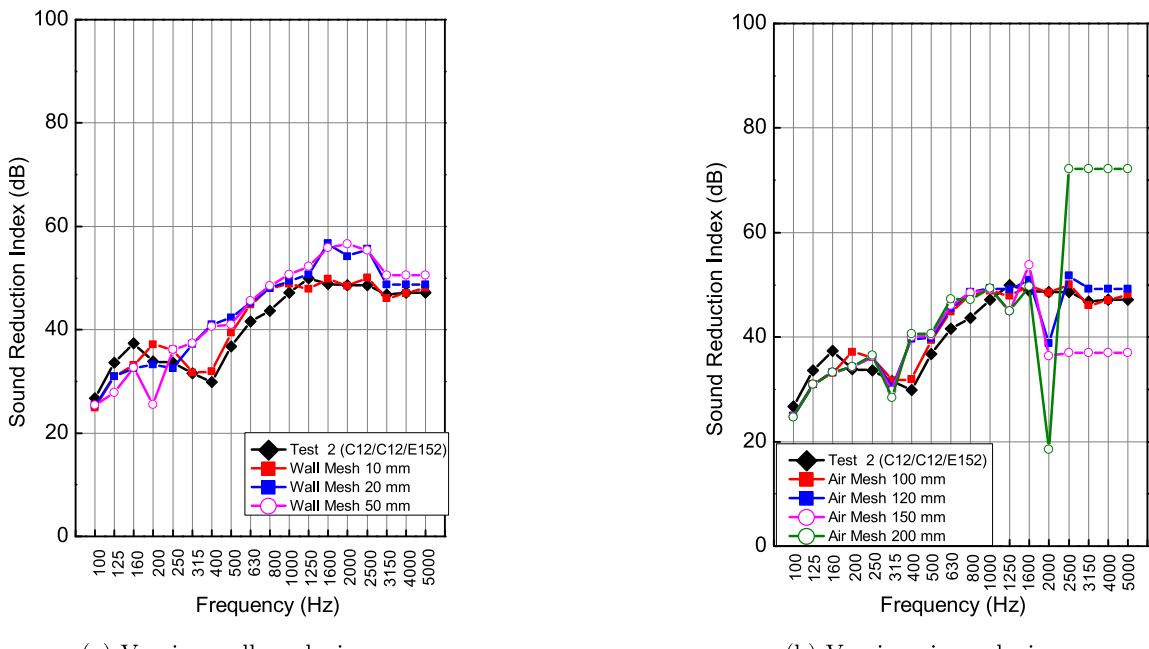


Fig. 11. FEA sound reduction index obtained for different mesh sizes of the walls and air inside two test rooms.

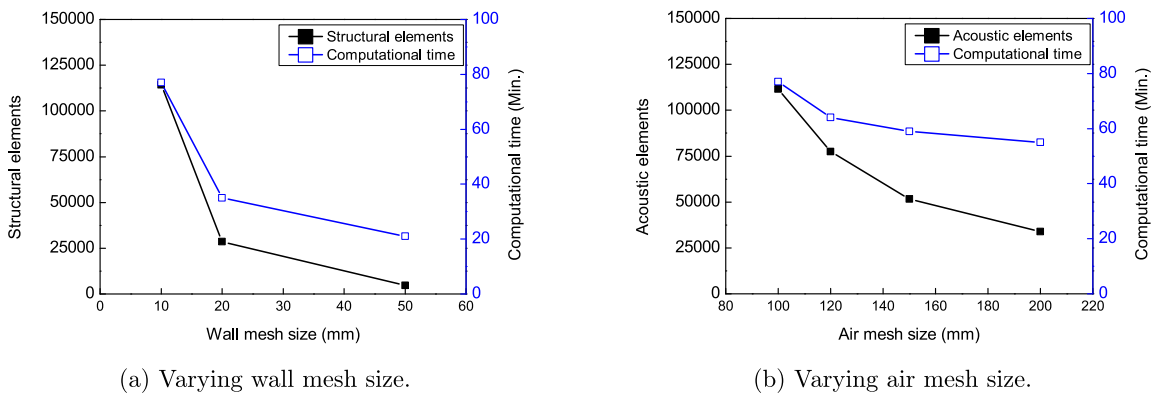


Fig. 12. The number of structural and acoustic elements for different mesh sizes of walls and air, and the computation times of FE models.

4.4. Validation

Figs. 13 and 14 compare sound reduction indices across one-third octave bands from 100 to 5000 Hz, based on field measurements and numerical simulations for Tests 1 and 2.

Test 1 showed a peak disparity of 7.1 dB at 500 Hz in the C12/M12/C6/E140 specimen, while the largest discrepancy in Test 2 was 8.9 dB at 5000 Hz for the C12/M6/C6/M6/E140 specimen. Overall, the results indicate a close alignment of sound reduction indices with experimental R -values.

The single number quantities R_w and $R_w + C$ for FE models of ten specimens in Test 1 and Test 2 were calculated and presented in Figs. 15 and 16. When compared with the experimental test results, the FE model outcomes exhibit good agreement.

Notable differences between the FEA and experimental single number quantities were observed as follows:

- For Test 1, the largest disparity observed for R_w was 4 dB in the C12/M12/C6/E140 specimen. In Test 2, the most significant discrepancy was 2 dB for most specimens, except for the C12/M12/C6/E140 specimen.
- Regarding $R_w + C$ values, Test 1 had the largest disparity of 3 dB in the C12/M12/C6/E140 specimen. In Test 2, the most significant discrepancy was 2 dB, notably in the C12/M18/E140 and C12/M12/C6/E140 specimens.

Overall, the predictive limitations of the FE models are particularly pronounced in specimens containing Melamine foam (see Fig. 14), especially at high frequencies (2000–5000 Hz). These discrepancies stem from model simplifications, material characterization constraints, and computational limitations.

The FE models assume perfect bonding between material layers and uniform material properties. However, in the experimental specimens, variations in adhesive bonding, surface roughness, and manufacturing imperfections may have introduced additional compliance and localized acoustic impedance mismatches, affecting the transmission loss. These inconsistencies are particularly influential at higher frequencies where small variations in material interfaces can lead to significant deviations in acoustic behavior.

The sound absorption characteristics of Melamine foam strongly depend on thickness, yet the specific values used in this study were not explicitly provided in the technical datasheet [25]. Instead, absorption coefficients were interpolated from available data, introducing potential uncertainties. Additionally, the foam's complex porous structure was modeled using impedance coefficients, simplifying its real-world behavior. These assumptions may lead to an overestimation of sound reduction, particularly at high frequencies.

The FE models employed PML to simulate non-reflective boundaries, which idealize the absorption of outgoing waves. In the actual experimental setup, however, the presence of diffusers and minor reflections from room surfaces could have led to variations in the measured sound reduction index, contributing to discrepancies between numerical and experimental results.

Moreover, mesh resolution limitations contribute to inaccuracies at high frequencies. The sensitivity analysis identified 100 mm as the optimal element size for air domains to balance computational efficiency and accuracy. However, this resolution does not satisfy the minimum requirement of at least six elements per wavelength [49], which is crucial for accurate wave propagation modeling. Insufficient air mesh density can reduce the accuracy of wave transmission simulations, particularly in the high-frequency range. Similar discrepancies have been observed in previous studies [47,50,51]. Although adaptive order functions were implemented to enhance computational precision, they may not fully compensate for mesh deficiencies, contributing to deviations in FE results at high frequencies.

4.5. Parametric study

A parametric FE analysis was conducted to predict the acoustic performance of Group 1 specimens, composed of layers with varying thicknesses of EPS and CRC. Each specimen had a surface area of 1.82 m^2 , consistent with Test 2. The study focused on evaluating the impact of varying the thicknesses of the CRC and EPS layers while maintaining a constant overall specimen thickness of 200 mm. Five FE models were analyzed: C6/C12/E164, C12/C12/E152, C6/C12/C12/E140, C6/C6/C12/C12/E128, and C6/C6/C12/C12/E116. In these configurations, the thickness of the EPS layer was systematically reduced from 164 mm to 116 mm, with

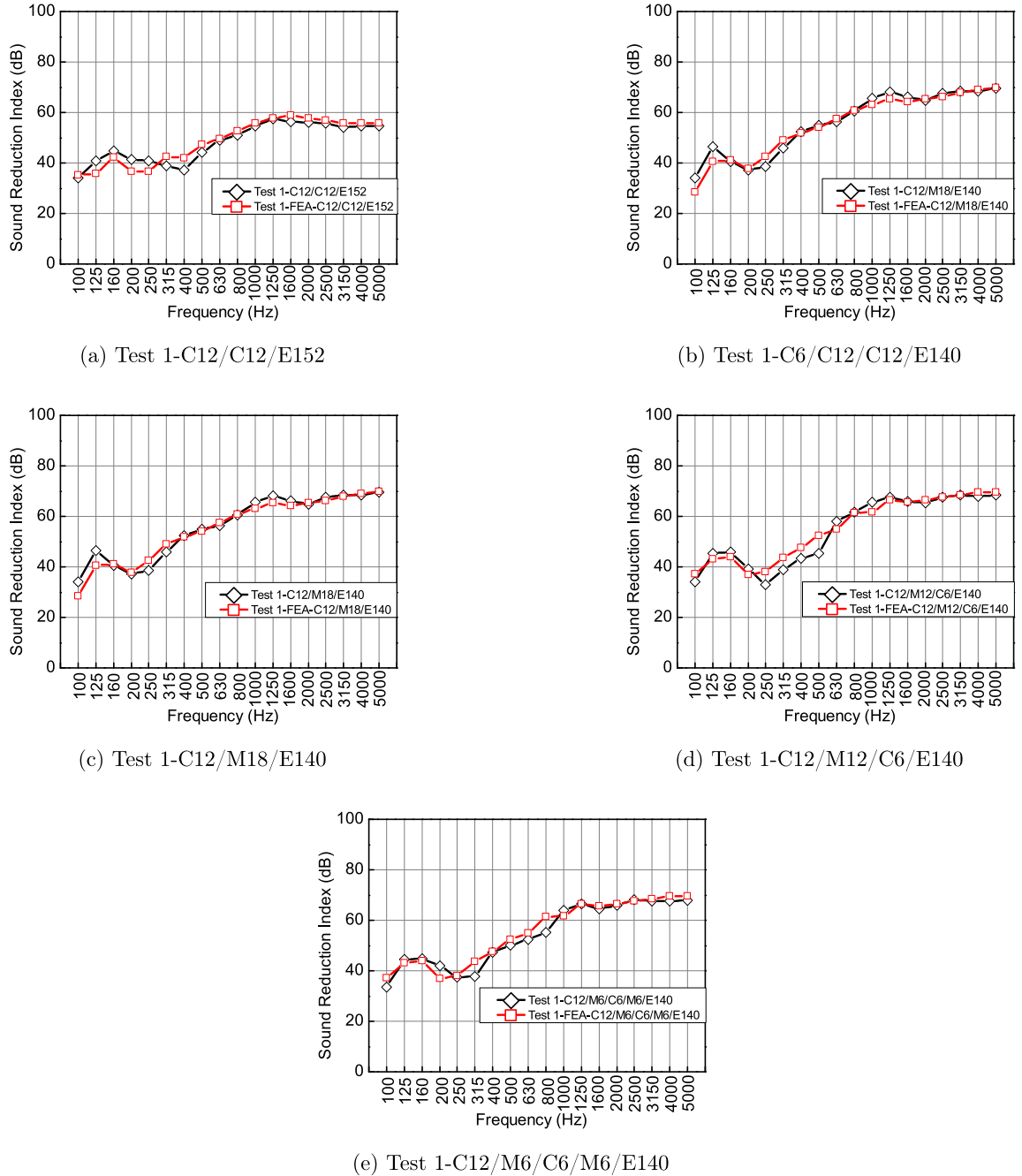


Fig. 13. Sound reduction index for different models obtained from FEA for specimens of Test 1.

specific values of 164 mm, 152 mm, 140 mm, 128 mm, and 116 mm. To maintain the total thickness of 200 mm, additional CRC layers were introduced to compensate for the reduced EPS thickness, with the added CRC layers having thicknesses of either 6 mm or 12 mm, depending on the model configuration. Detailed specimen configurations used in the parametric study are shown in Table 5.

Fig. 17a illustrates the relationship between EPS layer thickness variations and the sound reduction index of specimen configurations featuring an EPS core with external CRC layers. The figure shows that as the thickness of the EPS decreases, the sound reduction index for specimens in Group 1 increases across all frequencies.

Fig. 17b illustrates the variation in single-number quantities R_w and $R_w + C$ for the FE model as the EPS layer thickness increases from 116 mm to 164 mm. Both R_w and $R_w + C$ exhibit a decreasing trend, reducing from 49 dB to 43 dB and from 45 dB to 41 dB, respectively, due to the reduction in bending stiffness and surface mass, which directly influence the sound reduction index.

Although the relationship between EPS thickness and acoustic parameters is theoretically nonlinear due to the coupled effects of

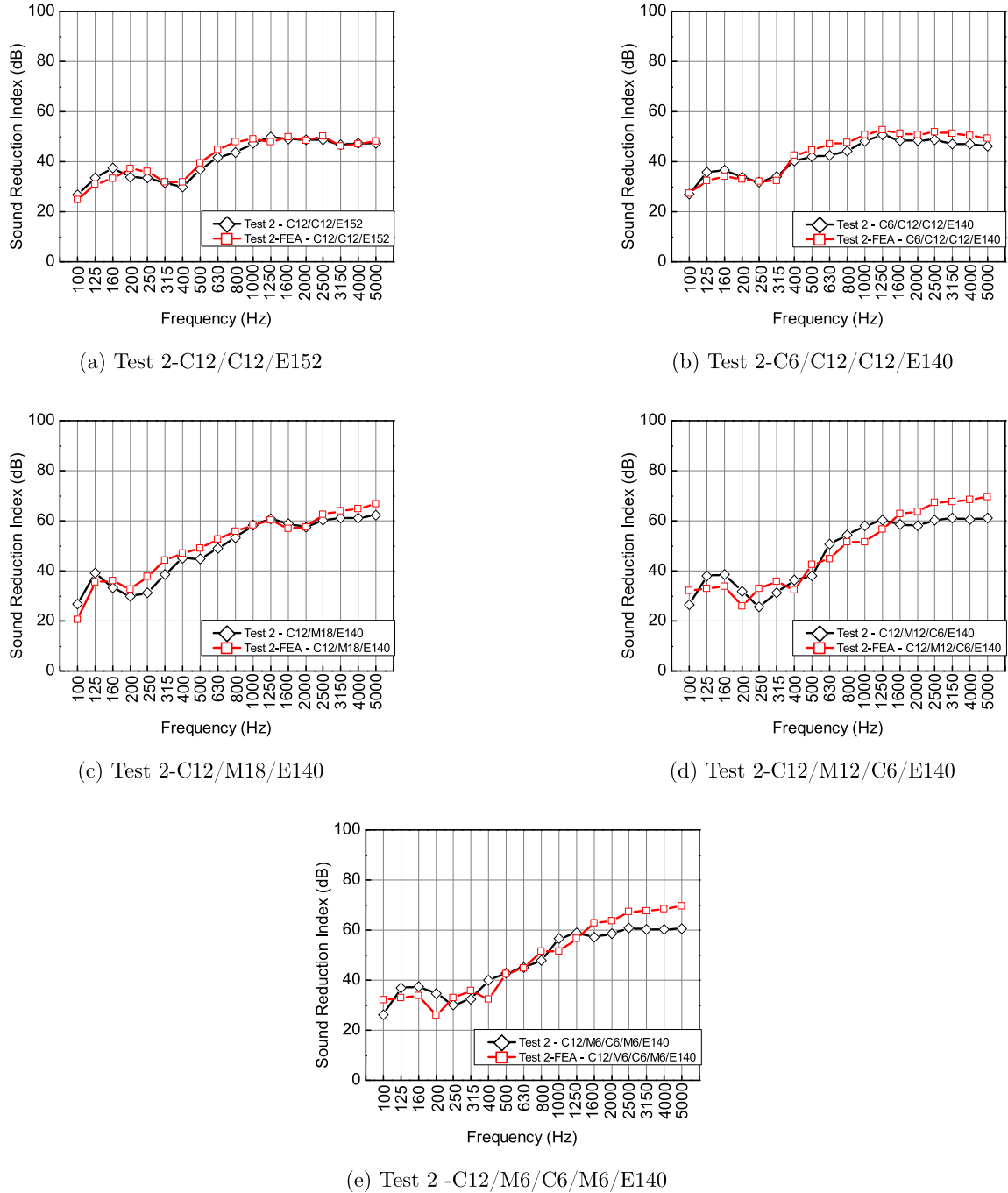
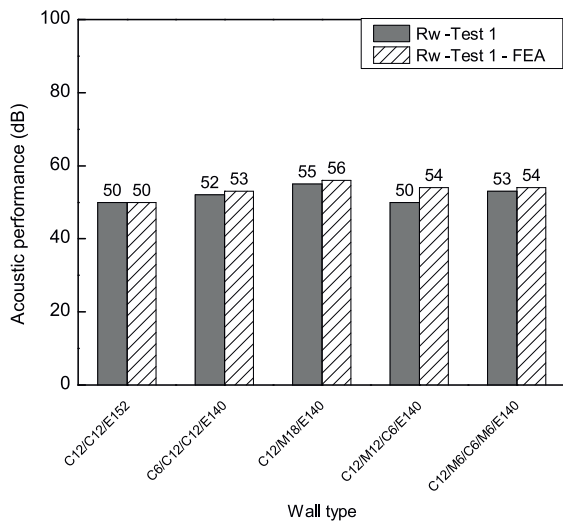
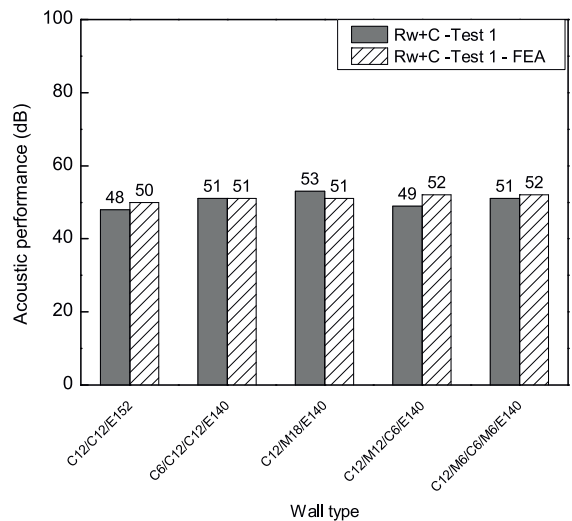
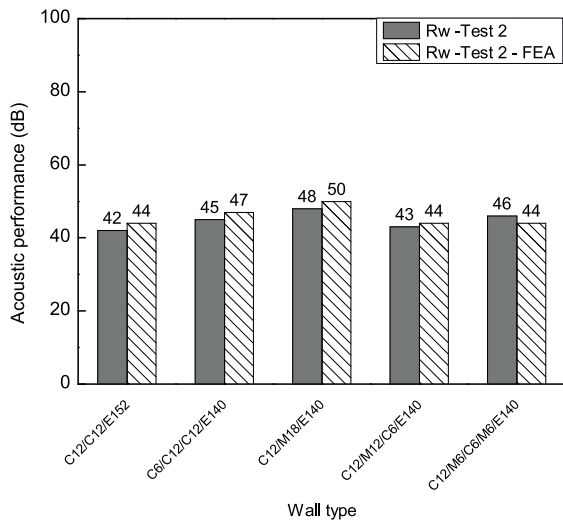
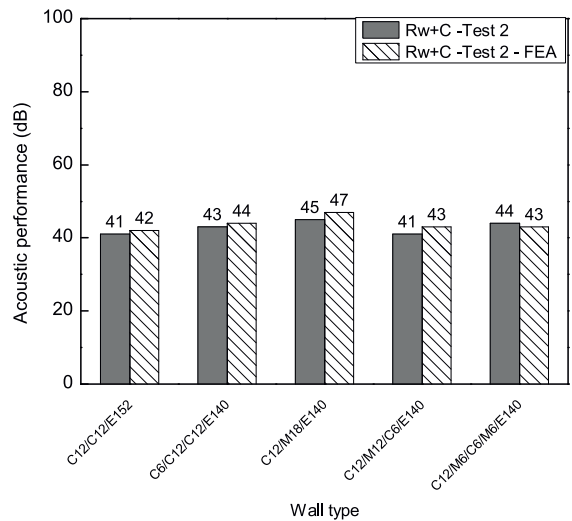


Fig. 14. Sound reduction index for different models obtained from FEA for specimens of Test 2.

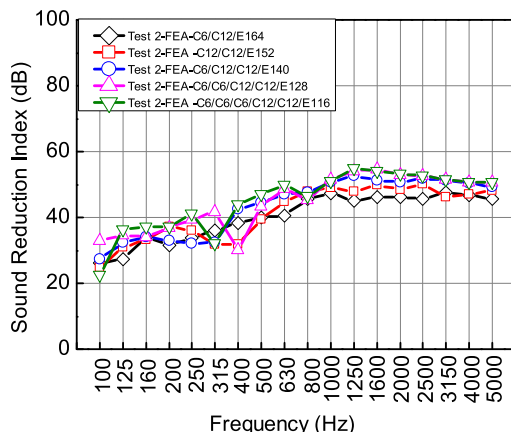
bending stiffness, surface mass, and damping, the numerical results indicate a strong correlation that can be closely approximated by a linear model. Linear regression analysis yielded R^2 values of 0.901 and 0.940 for R_w and $R_w + C$, respectively, demonstrating a high degree of predictive accuracy. Within the examined thickness range, the deviation from perfect linearity is minimal, allowing for a simplified linear estimation in practical applications. However, it is acknowledged that a more complex nonlinear model may be required when considering broader parameter variations or alternative material configurations.

These findings from the parametric study provide a foundation for determining and optimizing the acoustic performance of the specimens based on their configurations. Future parametric studies should incorporate variations in surface area to investigate the combined effects of geometry and material thickness on acoustic performance, aligning with the trends observed in the experimental results.

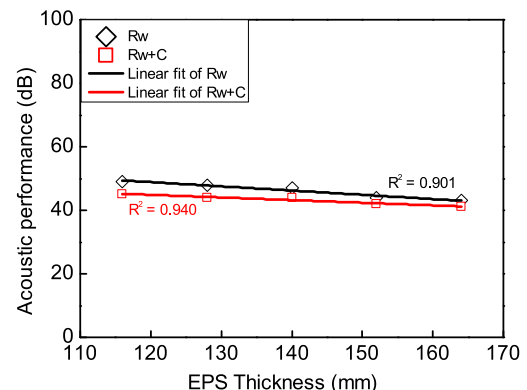
(a) Single number quantity R_w (b) Single number quantity $(R_w + C)$ Fig. 15. The overall acoustic performance of the specimens obtained from Test 1 ($S = 10.06 \text{ m}^2$) and FEA for five specimens.(a) Single number quantity R_w (b) Single number quantity $(R_w + C)$ Fig. 16. The overall acoustic performance of the specimens obtained from Test 2 ($S = 1.82 \text{ m}^2$) and FEA for five specimens.**Table 5**

Detailed specimen configurations used in the parametric study.

No.	Nomenclature	Thickness (mm)	EPS thickness (mm)	Composition
1	C6/C12/E164	200	164	C6mm+C12mm+E164mm+C12mm+C6mm
2	C12/C12/E152	200	152	C12mm+C12mm+E152mm+C12mm+C12mm
3	C6/C12/C12/E140	200	140	C6mm+C12mm+C12mm+E140mm+C12mm+C12mm+C6mm
4	C6/C6/C12/C12/E128	200	128	C6mm+C6mm+C12mm+C12mm+E128mm+C12mm+C12mm+C6mm+C6mm
5	C6/C6/C12/C12/E116	200	116	C6mm+C6mm+C6mm+C12mm+C12mm+E116mm+C12mm+C12mm+C6mm+C6mm+C6mm



(a) Sound reduction index.



(b) Single number quantities.

Fig. 17. Acoustic performance predicted by FE models for Group 1 specimens with varying thicknesses of the EPS layer.

5. Conclusions

This study investigated the sound insulation performance of novel thermal breaks incorporating various thermal insulation layers and Ultra-High-Performance Concrete (UHPC) cores. Through a combination of experimental tests and finite element analysis (FEA), the research identified key factors that influence acoustic properties in thermal breaks. While these findings provide valuable insights, they are limited to the context and scope of this study. The key conclusions are as follows:

- The results highlight that material composition and layering sequence significantly affect sound insulation across different frequency ranges. Increasing the thickness of dense materials like Cellulose Fiber Reinforced Cement (CRC) while reducing lightweight Expanded Polystyrene (EPS) improves low-to-mid frequency insulation. The strategic integration of porous materials, such as Melamine foam, further enhances mid-to-high frequency absorption, with multi-layered configurations demonstrating superior performance.
- Optimizing Melamine foam thickness is essential, as excessive thickness reduces structural stiffness and diminishes low-frequency insulation. This study found that a total Melamine foam thickness of 24 mm achieves an optimal balance between absorption and stiffness, enhancing overall acoustic efficiency.
- One effective strategy for improving sound insulation while maintaining thermal performance is increasing the mass of the system without significantly affecting its thermal resistance. Since higher mass improves low-frequency sound insulation, integrating high-density yet thermally efficient composites or introducing air cavities within the structure can help disrupt sound transmission while preserving insulation properties.
- The strong correlation between FEA predictions and experimental results confirms the reliability of numerical vibro-acoustic modeling for assessing sound insulation in thermal breaks. The deviation between predicted and observed results remained within an acceptable range of 2–3 dB, supporting the validity of the modeling approach.
- A parametric study demonstrated a nearly linear relationship between EPS thickness and sound insulation performance, providing a basis for optimizing thermal break configurations to meet specific acoustic requirements.

While this study primarily focused on sound insulation, future research should investigate the thermal implications of different material combinations. Further improvements should refine material layering, optimize mass-stiffness relationships, and explore novel composites that enhance both sound and thermal insulation. These findings underscore the importance of strategic material selection and structural design in optimizing thermal breaks, offering a foundation for improved acoustic and thermal performance in building applications.

6. Future research

Future research should explore the impact of temperature variations on the acoustic efficiency of the thermal break system. As buildings are exposed to fluctuating environmental conditions, factors such as thermal expansion, contraction, and material aging may affect performance over time. A coupled thermo-acoustic analysis would provide deeper insights into how these variations influence sound insulation.

Additionally, further studies should examine the long-term durability and mechanical stability of the thermal break under repeated loading. Continuous mechanical and environmental stressors could alter material properties, potentially affecting both structural integrity and acoustic efficiency. Large-scale experimental validation and field testing will be essential to ensure reliable real-world performance.

Addressing these aspects will contribute to the development of advanced thermal break systems with improved durability, sustainability, and acoustic efficiency, enhancing building performance and occupant comfort.

CRediT authorship contribution statement

Gayoon Lee: Writing – review & editing, Validation, Investigation, Data curation. **Yun-Seong Shin:** Writing – review & editing, Formal analysis. **Sungwoo Woo:** Writing – review & editing, Formal analysis. **Kihak Lee:** Writing – review & editing, Supervision, Resources, Project administration, Formal analysis, Conceptualization. **Tran-Van Han:** Writing – review & editing, Writing – original draft, Validation, Software, Methodology, Formal analysis, Data curation, Conceptualization.

Declaration of Competing Interest

The authors declare that they have no known competing financial interests or personal relationships that could have appeared to influence the work reported in this paper.

Data availability

The authors do not have permission to share data.

Acknowledgements

This work was supported by the National Research Foundation of Korea(NRF) grant funded by the Korea government (MSIT) (RS-2025-00518861).

Appendix A. Appendix

```
#Created on Wed Mar 6 2024
"""
@author: Han
"""

# Here is a Python code that attempts to replicate the standard procedure
# ISO 717-1 for calculating Rw.

# We shift the reference curve in increments of 0.1 dB towards the
# measured curve
# until the sum of unfavourable deviations is as large as possible but not
# more than 32 dB.

import numpy as np
import pandas as pd

# Load the Excel file and read the test data
df = pd.read_excel('calculate_rw.xlsx', sheet_name='1.86_calculate_FEM')

# Define the row range
a = 0 # Starting row (Python uses zero-based indexing)
b = 16 # Ending row (inclusive)
```

```
# Select the range of rows and a specific column to convert to a NumPy
# array
column_data = df.iloc[a:b][‘Test 2-FEA - C12/M12/C6/E140’].to_numpy()

# Actual measured R-values
# Replace with the actual measured R-values from 100 Hz to 3150 Hz in one-
# third-octave bands
R_values = column_data

# Reference curve values for the one-third-octave bands
reference_curve = np.array([33, 36, 39, 42, 45, 48, 51, 52, 53, 54, 55, 56
                           , 56, 56, 56])

# Function to calculate the weighted sound reduction index (Rw)
def calculate_rw(R_values, reference_curve, max_deviation=32):
    best_shift = 0
    smallest_deviation_sum = max_deviation
    for shift in np.arange(-100, 100, 0.1): # Shifting in increments of 0
                                                .1 dB
        # Shift the reference curve
        shifted_reference = reference_curve + shift
        # Calculate deviations
        deviations = R_values - shifted_reference
        # Calculate the sum of unfavourable deviations (only negative
                                                deviations)
        deviation_sum = np.sum(deviations[deviations < 0])
        deviation_sum = abs(deviation_sum)
        # Check if the sum of unfavourable deviations is within the
                                                allowed range
        # and if it is the largest possible without exceeding the maximum
        if deviation_sum > best_shift and deviation_sum <= max_deviation:
```

```

        best_shift = shift

        smallest_deviation_sum = deviation_sum

    # Calculate  $R_w$ : it is the value of the reference curve at 500 Hz after
    # shifting
     $R_w = \text{reference\_curve}[7] + \text{best\_shift}$  # Index 7 corresponds to 500 Hz
    return  $R_w$ , best_shift, smallest_deviation_sum

# Calculate  $R_w$ 
 $R_w$ , best_shift, smallest_deviation_sum = calculate_rw( $R_{\text{values}}$ ,
    reference_curve)

 $R_w$ , best_shift, smallest_deviation_sum
print(f"Weighted Sound Reduction Index ( $R_w$ ): {Rw}")

```

References

- [1] S.M.A. Qaidi, Y.Z. Dinkha, J.H. Haido, M.H. Ali, B.A. Tayeh, Engineering properties of sustainable green concrete incorporating eco-friendly aggregate of crumb rubber: a review, *J. Clean. Prod.* 324 (2021) 129251, <https://doi.org/10.1016/j.jclepro.2021.129251>.
- [2] S.M.A. Qaidi, B.A. Tayeh, A.M. Zeyad, A.R.G. de Azevedo, H.U. Ahmed, W. Emad, Recycling of mine tailings for the geopolymers production: a systematic review, *Case Stud. Constr. Mater.* 16 (2022) e00933, <https://doi.org/10.1016/j.cscm.2022.e00933>.
- [3] V. Harish, A. Kumar, A review on modeling and simulation of building energy systems, *Renew. Sustain. Energy Rev.* 56 (2016) 1272–1292, <https://doi.org/10.1016/j.rser.2015.12.040>.
- [4] F. Ascione, N. Bianco, G.M. Mauro, D.F. Napolitano, Building envelope design: Multi-objective optimization to minimize energy consumption, global cost and thermal discomfort. application to different italian climatic zones, *Energy* 174 (2019) 359–374, <https://doi.org/10.1016/j.energy.2019.02.182>.
- [5] G. Evola, G. Margani, L. Marletta, Energy and cost evaluation of thermal bridge correction in mediterranean climate, *Energy Build.* 43 (2011) 2385–2393, <https://doi.org/10.1016/j.enbuild.2011.05.028>.
- [6] S. Real, M.G. Gomes, A.M. Rodrigues, J.A. Bogas, Contribution of structural lightweight aggregate concrete to the reduction of thermal bridging effect in buildings, *Constr. Build. Mater.* 121 (2016) 460–470, <https://doi.org/10.1016/j.conbuildmat.2016.06.018>.
- [7] A.B. Larbi, Statistical modelling of heat transfer for thermal bridges of buildings, *Energy Build.* 37 (2005) 945–951, <https://doi.org/10.1016/j.enbuild.2004.12.013>.
- [8] L. Simwanda, C. Kahanji, F. Ali, Numerical modelling, parametric analysis and design of upfrc beams exposed to fire, volume 52. *Structures*, Elsevier, 2023, pp. 1–16, <https://doi.org/10.1016/j.istruc.2023.03.155>. volume 52.
- [9] S. Ng, B.P. Jelle, Y. Zhen, Ó.H. Wallevik, Effect of storage and curing conditions at elevated temperatures on aerogel-incorporated mortar samples based on uphc recipe, *Constr. Build. Mater.* 106 (2016) 640–649, <https://doi.org/10.1016/j.conbuildmat.2015.12.162>.
- [10] N.H. Cuong, H. An, H.V. Tran, S. An, K. Lee, Structural test and analyses of uphc horizontal connection with shear keys for slab-external pc wall, *Constr. Build. Mater.* 419 (2024) 135410, <https://doi.org/10.1016/j.conbuildmat.2024.135410>.
- [11] V. Kodur, S. Banerji, R. Solhmirzaei, Effect of temperature on thermal properties of ultrahigh-performance concrete, *J. Mater. Civ. Eng.* 32 (2020) 04020210, [https://doi.org/10.1061/\(ASCE\)MT.1943-5533.0003286](https://doi.org/10.1061/(ASCE)MT.1943-5533.0003286).
- [12] M. Abid, X. Hou, W. Zheng, R.R. Hussain, High temperature and residual properties of reactive powder concrete—a review, *Constr. Build. Mater.* 147 (2017) 339–351, <https://doi.org/10.1016/j.conbuildmat.2017.04.083>.
- [13] S. Aghasizadeh, B.M. Kari, R. Fayaz, Thermal performance of balcony thermal bridge solutions in reinforced concrete and steel frame structures, *J. Build. Eng.* 48 (2022) 103984, <https://doi.org/10.1016/j.jobe.2021.103984>.
- [14] Y. Kim, J. Park, M. Joo, Y. Oh, A study on the traffic noise level of apartment and the validity of the regulation scheme, *J. KIAEBS* 4 (2010) 111.
- [15] H.K. Park, H. Kim, Acoustic insulation performance of improved airtight windows, *Constr. Build. Mater.* 93 (2015) 542–550, <https://doi.org/10.1016/j.conbuildmat.2015.05.058>.
- [16] V. Hongisto, P. Saarinen, R. Alakoiru, J. Hakala, Acoustic properties of commercially available thermal insulators- an experimental study, *J. Build. Eng.* 54 (2022) 104588, <https://doi.org/10.1016/j.jobe.2022.104588>.
- [17] D. Urbán, N.B. Roonen, P. Zat'ko, H. Muellner, C. Glorieux, Influence of the dynamic stiffness of external thermal insulation on the sound insulation of walls, [\(http://www.euronoise2018.eu/\)](http://www.euronoise2018.eu/).(2018).
- [18] U. Berardi, G. Iannace, Acoustic characterization of natural fibers for sound absorption applications, *Build. Environ.* 94 (2015) 840–852, <https://doi.org/10.1016/j.buildenv.2015.05.029>.
- [19] E. Moretti, E. Belloni, F. Agosti, Innovative mineral fiber insulation panels for buildings: thermal and acoustic characterization, *Appl. Energy* 169 (2016) 421–432, <https://doi.org/10.1016/j.apenergy.2016.02.048>.
- [20] D. Oliva, V. Hongisto, Sound absorption of porous materials—accuracy of prediction methods, *Appl. Acoust.* 74 (2013) 1473–1479, <https://doi.org/10.1016/j.apacoust.2013.06.004>.
- [21] V. Hongisto, M. Lindgren, R. Helenius, Sound insulation of double walls—an experimental parametric study, *Acta Acust. U. Acust.* 88 (2002) 904–923.
- [22] V. Hongisto, A case study of flanking transmission through double structures, *Appl. Acoust.* 62 (2001) 589–599, [https://doi.org/10.1016/S0003-682X\(00\)00061-X](https://doi.org/10.1016/S0003-682X(00)00061-X).

- [23] V. Hongisto, P. Virjonen, H. Maula, P. Saarinen, J. Radun, Impact sound insulation of floating floors: a psychoacoustic experiment linking standard objective rating and subjective perception, *Build. Environ.* 184 (2020) 107225, <https://doi.org/10.1016/j.buildenv.2020.107225>.
- [24] N.H. Cuong, K.J. Young, S. An, H. Kim, J. Shin, K. Lee, Structural performance and numerical analysis of parapet thermal bridge solutions with cellulose fiber reinforced cement board and different reinforcement layouts for residential buildings, *Eng. Struct.* 329 (2025) 119713, <https://doi.org/10.1016/j.engstruct.2025.119713>.
- [25] Nordic Foam by Linde+Larsen, Technical datasheet – basotect g+ (black), 2020. (<https://nordicfoam.eu/wp-content/uploads/2020/06/Basotect-G-Technical-datasheet-LindeLarsen-June-2020.pdf>).
- [26] E. DIN, 354: acoustics-measurement of sound absorption in a reverberation room (iso 354: 2003), Ger. Version EN ISO 354 (2003) 2003.
- [27] T.M. Kim, J.T. Kim, J.S. Kim, Effect of structural vibration and room acoustic modes on low frequency impact noise in apartment house with floating floor, *Appl. Acoust.* 142 (2018) 59–69, <https://doi.org/10.1016/j.apacoust.2018.07.034>.
- [28] N.H. Ramli Sulong, S.A.S. Mustapa, M.K. Abdul Rashid, Application of expanded polystyrene (eps) in buildings and constructions: a review, *J. Appl. Polym. Sci.* 136 (2019) 47529, <https://doi.org/10.1002/app.47529>.
- [29] Á. Lakatos, Z. Kovács, Comparison of thermal insulation performance of vacuum insulation panels with eps protection layers measured with different methods, *Energy Build.* 236 (2021) 110771, <https://doi.org/10.1016/j.enbuild.2021.110771>.
- [30] Y. Wang, Z. Chen, Y. Lu, L. Yang, T. Xu, H. Wu, J. Zhang, L. He, A review of application, modification, and prospect of melamine foam, *Nanotechnol. Rev.* 12 (2023) 20230137, <https://doi.org/10.1515/ntrrev-2023-0137>.
- [31] H. Singh, R. Gupta, Influence of cellulose fiber addition on self-healing and water permeability of concrete, *Case Stud. Constr. Mater.* 12 (2020) e00324, <https://doi.org/10.1016/j.cscm.2019.e00324>.
- [32] N. Saba, M. Jawaid, M. Paridah, O. Al-Othman, A review on flammability of epoxy polymer, cellulosic and non-cellulosic fiber reinforced epoxy composites, *Polym. Adv. Technol.* 27 (2016) 577–590, <https://doi.org/10.1002/pat.3739>.
- [33] H. Choi, Y.C. Choi, Setting characteristics of natural cellulose fiber reinforced cement composite, *Constr. Build. Mater.* 271 (2021) 121910, <https://doi.org/10.1016/j.conbuildmat.2020.121910>.
- [34] M. Long, *Architectural acoustics*, Elsevier, 2005.
- [35] O.A. Hassan, *Building acoustics and vibration: theory and practice*, World Scientific Publishing Company, 2009.
- [36] E. ISO, 10140-4: Laboratory measurement of sound insulation of building elements-part 4: Measurement procedures and requirements, International Organization for Standardization, Geneva (2021).
- [37] E. ISO, 10140-2: Acoustics-laboratory measurement of sound insulation of building elements-part 2: Measurement of airborne sound insulation, International Organization for Standardization, Geneva (2021).
- [38] J. Nurzyński, Sound insulation of lightweight external frame walls and the acoustic effect of additional thermal insulation, *Appl. Acoust.* 190 (2022) 108645, <https://doi.org/10.1016/j.apacoust.2022.108645>.
- [39] I. ISO, 717-1; acoustics—rating of sound insulation in buildings and of building elements—part 1: Airborne sound insulation, International Organization for Standardization: Geneva, Switzerland (2020).
- [40] D. Bies, C. Hansen, *Engineering noise control: Theory and practice*, (paperback), 2009.
- [41] P. Ruggeri, F. Peron, N. Granzotto, P. Bonfiglio, A combined experimental and analytical approach for the simulation of the sound transmission loss of multilayer glazing systems, *Build. Acoust.* 22 (2015) 177–192, <https://doi.org/10.1260/1351-010X.22.3-4.177>.
- [42] N. Granzotto, A. Di Bella, E.A. Piana, Prediction of the sound reduction index of clay hollow brick walls, *Build. Acoust.* 27 (2020) 155–168, <https://doi.org/10.1177/1351010X20903144>.
- [43] KATS, Ks f 2862; method of evaluating the air transmitting sound insulation performance of building and building members, Seoul: Korean Agency for Technology and Standards, Ministry of Industry and Resources (2002).
- [44] W. Utley, B. Fletcher, The effect of edge conditions on the sound insulation of double windows, *J. Sound Vib.* 26 (1973) 63–72, [https://doi.org/10.1016/S0022-460X\(73\)80205-6](https://doi.org/10.1016/S0022-460X(73)80205-6).
- [45] S.N. Shoukry, G.W. William, B. Downie, M.Y. Riad, Effect of moisture and temperature on the mechanical properties of concrete, *Constr. Build. Mater.* 25 (2011) 688–696, <https://doi.org/10.1016/j.conbuildmat.2010.07.020>.
- [46] P. Siemens, Simcenter 3d, 2023.
- [47] A. Arjunan, C. Wang, K. Yahiaoui, D. Mynors, T. Morgan, V.B. Nguyen, M. English, Development of a 3d finite element acoustic model to predict the sound reduction index of stud based double-leaf walls, *J. Sound Vib.* 333 (2014) 6140–6155, <https://doi.org/10.1016/j.jsv.2014.06.032>.
- [48] J.-P. Berenger, *A perfectly matched layer for the absorption of electromagnetic waves*, *J. Comput. Phys.* 114 (1994) 185–200.
- [49] Siemens, *Acoustics User's Guide*, Siemens Product Lifecycle Management Software, 2016.
- [50] A. Arjunan, C. Wang, K. Yahiaoui, D. Mynors, T. Morgan, M. English, Finite element acoustic analysis of a steel stud based double-leaf wall, *Build. Environ.* 67 (2013) 202–210, <https://doi.org/10.1016/j.buildenv.2013.05.021>.
- [51] J. Zhang, D. Yao, R. Wang, X. Xiao, Vibro-acoustic modelling of high-speed train composite floor and contribution analysis of its constituent materials, *Compos. Struct.* 256 (2021) 113049, <https://doi.org/10.1016/j.compstruct.2020.113049>.